ACS Catalysis

Research Article

pubs.acs.org/acscatalysis

Layered $Co(OH)_2$ Deposited Polymeric Carbon Nitrides for Photocatalytic Water Oxidation

Guigang Zhang, Shaohong Zang, and Xinchen Wang*

State Key Laboratory of Photocatalysis on Energy and Environment, College of Chemistry, Fuzhou University, Fuzhou, 350002, People's Republic of China

Supporting Information

ABSTRACT: Here we report a facile impregnation synthesis of layered $Co(OH)_2$ deposited with g-C_3N_4 while the pH value is adjusted by using ammonia solution for photocatalytic water oxidation with UV−vis and visible light illumination. This surface modification not only accelerates the interface transfer rate of charge carriers but also reduces the excessive energy barrier for O−O formation, thus leading to enhanced reaction kinetics for photocatalytic water oxidation. The optimum oxygen evolution rates (OERs) of the $Co(OH)_2$/g-C_3N_4 sample reached 27.4 and 7.1 μmol h^{-1} under UV−vis (λ >300 nm) and visible light (λ >420 nm) irradiation, which are 5.5 and 7 times faster than those for pristine g-C_3N_4, respectively. These results underline the possibility for the development of effective, robust, and earth-abundant WOCs for the promotion of water-splitting photocatalysis by sustainable g-C_3N_4 polymer photocatalysts.

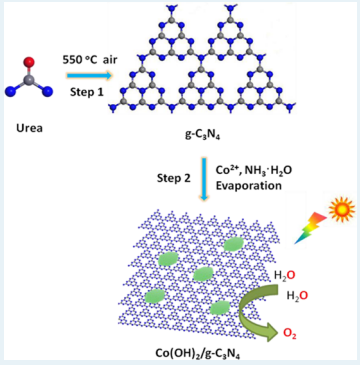

KEYWORDS: *photocatalysis, graphitic carbon nitride, water oxidation, heterojunction, cobalt hydroxide*

INTRODUCTION

Water splitting has long been considered as one of the carbon-neutral strategies to ameliorate stringent energy demands and environmental sustainability since the first report of TiO_2 equipped in a electrochemical cell by Fujishima and Honda in 1972.[1] Hydrogen, which is capable of reducing our reliance on fossil fuels, has been regarded as a promising carbon-neutral alternative and an ideal clean fuel carrier.[2] However, the main obstacle of large-scale hydrogen production via water splitting is the slow kinetics of water oxidation owing to complex multielectron oxidation process and huge activation energy barrier for O−O bond formation.[3] Currently, the most effective water oxidation catalysts (WOCs) are Ru- and Ir-based oxides, despite their limited availability and unacceptable cost.[4]

To achieve solar-photon-driven water oxidation effectively, a suitable WOC containing earth-abundant elements is required.[5] Cobalt-based oxides have shown promising potential for photocatalytic water oxidation in recent research. For example, porous cobalt phosphate (denoted as Co-Pi) or spinel Co_3O_4 has been incorporated with several inorganic metal oxides or polymeric substrate materials such as Fe_2O_3, $BiVO_4$, WO_3, and g-C_3N_4.[6] Interestingly, significant improvement in promoting the water oxidation rate can be obtained by reducing the recombination rate of the charge carriers, decreasing the energy barrier of the water oxidation kinetics, accelerating the charge distribution, and increasing band-bending.[6] However, until now, the efficiency of photocatalytic water oxidation has still been moderate, which extremely restricts its commercial utilization and industrial application. Thus, tremendous efforts are still needed to improve their catalytic performance.

Recently, Lin and Boettcher have described a creative approach to resolve the behavior of WOCs on semiconductor surfaces by probing them in situ.[7] It is remarkable to observe that the water oxidation performance of porous $Ni(OH)_2$ is higher than that of compact IrO_2 when either of them is deposited on a model TiO_2 substrate, respectively. The better performance of $Ni(OH)_2/TiO_2$ system is mainly ascribed to the shift in the chemical potential of $Ni(OH)_2$ catalyst to positive values by ~0.6 V as a result of the formation of $Ni(OH)_2$/NiOOH film. In addition, nanoporous $BiVO_4$ photoanodes deposited with dual-layer oxygen evolution catalysts (FeOOH and NiOOH) have recently been demonstrated to achieve a photocurrent density of 2.73 mA cm^{-2} at a potential as low as 0.6 V versus RHE. This is mainly due to the reduced interface recombination at the $BiVO_4$/OEC junction while a more favorable Helmholtz layer potential drop is created at the OEC/electrolyte junction.[8] Thus, it is recommended to develop a novel heterojunction by constructing a metal hydroxide with proper light-energy transducers for highly effective solar-driven water oxidation.

Very recently, intense attention has been given to a melon-based two-dimensional (2D) conjugated polymer, graphitic carbon nitride (generally termed as g-C_3N_4 for simplicity), which has been demonstrated to be a promising visible-light-responsive candidate for water splitting due to its unique electronic band structure and good (photo)chemical stability.[9] Although this species exhibits excellent hydrogen production,

Received: October 14, 2014
Published: December 22, 2014

DOI: 10.1021/cs502002u
ACS Catal. 2015, 5, 941−947

CO_2 reduction, and pollution purification performance, its water oxidation ability is particularly limited. Due to the fact that the valence band hybridization is relatively negative, the charge carrier distribution is torpid and the water oxidation kinetics is lethargic.[10−12] To enhance the water oxidation performance, either controlling the polymerization process or accelerating the water oxidation kinetics is a feasible strategy.[6d,10c] Moreover, currently, persistent efforts are still needed to investigate the determinate factor to reduce the interface recombination rate of the g-C_3N_4/OEC junction. Toward this goal, we report an adaptive polymer/inorganic junction between g-C_3N_4 and cobalt hydroxide, aiming to gather more details of the g-C_3N_4/OEC junction for promoting the thermodynamics and kinetics of water oxidation. The adaptive layered junction was fabricated via a facile in situ impregnation strategy based on a bottom-up synthesis of layered $Co(OH)_2$ at the interface of the g-C_3N_4 graphitic layer.

EXPERIMENTAL SECTION

Materials. All chemicals are of analytical grade and were used as received without further purification.

Synthesis of g-C_3N_4. The typical g-C_3N_4 photocatalyst was prepared by a traditional thermal polymerization strategy as reported previously. In a typical procedure, 5 g of urea was placed in a crucible with a cover, and then it was annealed at 550 °C for 2 h in the air. The final yellow powder was then collected. It was denoted as g-C_3N_4.

Synthesis of $Co(OH)_2$/g-C_3N_4. The hybridized materials were obtained by an immersion method. In a typical procedure, 1 g of as-prepared g-C_3N_4 was immersed into 5 mL aqueous solutions containing different amounts of $Co(NO_3)\cdot 6H_2O$. These were then mixed with stirring and ultrasonication for 10 min. Thereafter, 1 mL of aqueous ammonia was added dropwise into the above solution, and a green precipitate was immediately formed. The final resultant sample was obtained after evaporation and drying in an oven at 80 °C for 12 h.

Characterization. XRD measurements were performed on a Bruker D8 Advance diffractometer with Cu Kα_1 radiation. The UV/vis spectra were recorded on a Varian Cary 500 Scan UV/vis system. TEM was performed with an FEI Tencai 20 microscope. X-ray photoelectron spectroscopy (XPS) data were obtained on a Thermo ESCALAB250 instrument with a monochromatized Al Kα line source (200 W). Photoluminescence spectra were recorded on an Edinburgh FI/FSTCSPC 920 spectrophotometer. Electrochemical measurements were conducted with a BAS Epsilon Electrochemical System in a conventional three-electrode cell, using a Pt plate as the counter electrode and an Ag/AgCl electrode (3 M KCl) as the reference electrode. The working electrode was prepared on F-doped tin oxide (FTO) glass that was cleaned by sonication in ethanol for 30 min and dried at 353 K. The boundary of the FTO glass was protected using Scotch tape. A 5 mg sample was dispersed in 1 mL of DMF by sonication to give a slurry mixture. The slurry was spread onto pretreated FTO glass. After air drying, the working electrode was further dried at 393 K for 2 h to improve adhesion. Then, the Scotch tape was removed, and the uncoated part of the electrode was isolated with epoxy resin. The electrolyte was 0.2 M Na_2SO_4 aqueous solution without additive (pH 6.8). The scan rate was 50 mV/s.

Photocatalytic Test for Water Oxidation. Photocatalytic O_2 production was carried out in a Pyrex top-irradiation reaction vessel connected to a glass closed gas circulation system. For each reaction, 50 mg of catalyst powder was well dispersed in an aqueous solution (100 mL) containing $AgNO_3$ (0.01 M) as an electron acceptor and La_2O_3 (0.2 g) as a pH buffer agent. The reaction solution was evacuated several times to remove air completely prior to irradiation with a 300 W Xeon lamp with a working current of 15 A (Shenzhen ShengKang Technology Co., Ltd., Guangdong, People's Republic of China; LX300F). The wavelength of the incident light was controlled by applying some appropriate long-pass cutoff filters. The reaction solution was maintained at room temperature by a flow of cooling water during the reaction. The evolved gases were analyzed in situ by a gas chromatograph equipped with a thermal conductive detector (TCD) and a 5 Å molecular sieve column, using argon as the carrier gas. The selectivity for oxygen evolution was calculated by using the following equation: S = (amount of evolved O_2)/((amount of evolved O_2) + (amount of evolved N_2)).

RESULTS AND DISCUSSION

In order to investigate the physicochemical properties of the as-prepared samples in detail, a series of characterizations, including XRD, XPS, TEM, DRS, BET, and PL, have been carried out carefully. First, to certify the successful fabrication of the layered $Co(OH)_2$ on g-C_3N_4, the as-prepared nanocomposite was examined by powder XRD characterizations. In Figure 1, all of the samples show two distinct XRD peaks at

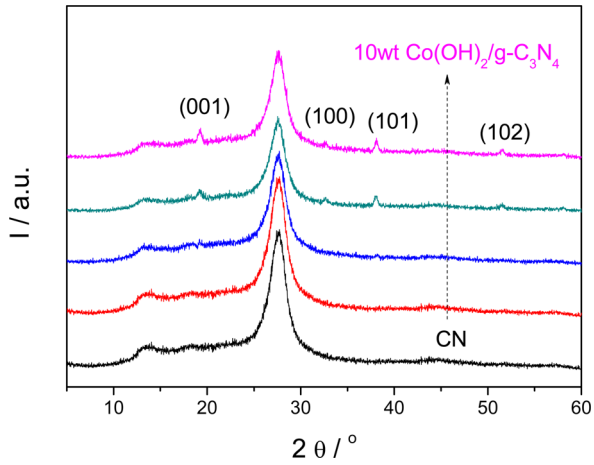

Figure 1. Powder XRD patterns of pure and $Co(OH)_2$-modified g-C_3N_4 samples.

2θ = 13.0 and 27.4°. The former peak is related to the in-plane structural repeating units of tri-*s*-triazine, while the latter is attributed to the (002) plane with graphitic stacking.[13] In comparison with pure g-C_3N_4, no evident difference can be observed except for the decrease in peak intensity. The two peaks are typical diffraction signals of graphitic carbon nitride materials. This indicates that the basic graphitic structure of g-C_3N_4 does not alternate after the surface modification treatment. When the $Co(OH)_2$ loading contents increased, four individual peaks gradually appeared at 19.1, 32.5, 38, and 51.4°, corresponding to (001), (100), (101), and (102), respectively. They are determined as the typical signals for $Co(OH)_2$ (PDF: #30-0443) with a layered crystal structure.[14] This well illustrates the successful fabrication of layered $Co(OH)_2$ nanocrystals on the surface of the g-C_3N_4 semiconductor with a layered polymeric structure.

DOI: 10.1021/cs502002u
ACS Catal. 2015, 5, 941−947

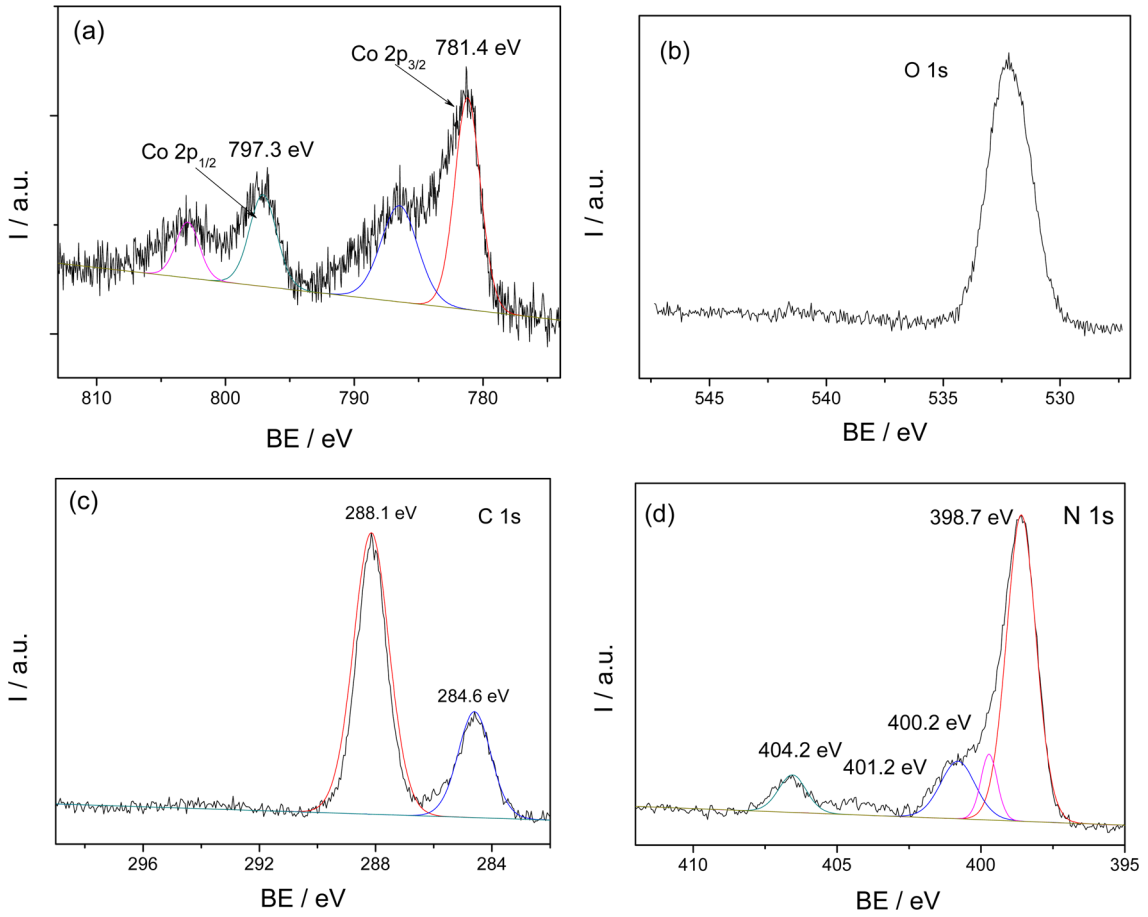

Figure 2. High-resolution XPS characterization of Co 2p (a), O 1s (b), C 1s (c), and N 1s (d) for a 3 wt % $Co(OH)_2/g\text{-}C_3N_4$ sample.

The existence of $Co(OH)_2$ can be further certified by high-resolution XPS analysis of Co 2p. In Figure 2a, the high XPS resolution of Co 2p can be deconvoluted into two pairs of individual peaks at 781.4 and 797.3 eV, respectively, which are identified as the major binding energies of Co^{2+} in $Co(OH)_2$.[14] The binding energy of O 1s at 532.2 eV is attributed to the surface hydroxyl groups. Once again, this demonstrates the formation of $Co(OH)_2$ via the facile wet-chemistry strategy. We also carried out high-resolution of XPS analysis of C 1s and N 1s. In Figure 2c, two single peaks at 284.6 and 288.1 eV can be found for C 1s. The first peak is a standard carbon specialized for the sample, whereas the latter peak is a typical signal for sp^2-hybridized carbon which is determined as the N−C═N backbone of the $g\text{-}C_3N_4$.[15] In Figure 2d, the N 1s peak can be deconvoluted into four peaks at 398.7, 400.2, 401.2, and 404.2 eV, respectively. The first peak is the classical peak of sp^2-hybridized nitrogen in the form of C−N═C, while the second peak at 400.2 eV is related to $N-(C)_3$ groups. These two nitrogen species together with the sp^2-bonded carbon make up the heptazine heterocyclic (C_6N_7) units of polymeric $g\text{-}C_3N_4$.[16] The weak peak with a binding energy of 401.2 eV corresponds to the surface uncondensed C−N−H functional groups, while the greatest bonding energy results from charging effects or positive charge localization in the heterocycles. The C 1s and N 1s spectra are both similar to that of pure $g\text{-}C_3N_4$, which indicates the incorporation of layered $Co(OH)_2$ nanocrystals on the substrate material.

To obtain more details about the texture and morphology of the hybridized materials, high-resolution TEM (HR-TEM) characterizations were then carried out. Figure 3a shows a piece of a typical silk nanosheet of graphitic carbon nitride. No evident large-particle accumulation can be seen on the surface of the two-dimensional (2D) $g\text{-}C_3N_4$ photocatalyst. Further enlargement of the selected area is shown in Figure 3b,c. It is clear that a well-fabricated layered $Co(OH)_2$ sheet is connected with the 2D carbon nitride graphitic layer. In Figure 3d, the obvious lattice fringe with a *d* spacing of 0.4418 nm is in good agreement with the (001) facet of XRD analysis. The N_2 adsorption−desorption isotherms of $g\text{-}C_3N_4$ and 3 wt % $Co(OH)_2/g\text{-}C_3N_4$ samples have been investigated. As shown in Figure S1 (Supporting Information), no evident changes are observed for the two curves, indicating little difference can be revealed after depositing $Co(OH)_2$ on the interface of $g\text{-}C_3N_4$. The BET surface areas for $g\text{-}C_3N_4$ and 3 wt % $Co(OH)_2/g\text{-}C_3N_4$ are 65 and 61 $m^2\ g^{-1}$. The slightly decreased surface area is due to the loading of $Co(OH)_2$ nanoparticles. The good deposition of $Co(OH)_2$ on $g\text{-}C_3N_4$ nanosheets contributes to accelerate the charge carrier distribution, separation, and migration rate. Thus, we have investigated the physicochemical properties of the as-prepared hybridized materials in detail.

The optical properties of the as-prepared hybridized solids were checked by room-temperature photoluminescence (PL) and UV−vis diffuse reflection spectra (DRS), respectively. In Figure 4a, the optical absorption band edge enhanced from 450 to 700 nm as the $Co(OH)_2$ content increased. However, few differences arising from the inherent band structure of the $g\text{-}C_3N_4$ polymer could be seen after the modification. This is mainly because the triazine-based graphitic structure does not

DOI: 10.1021/cs502002u
ACS Catal. 2015, 5, 941−947

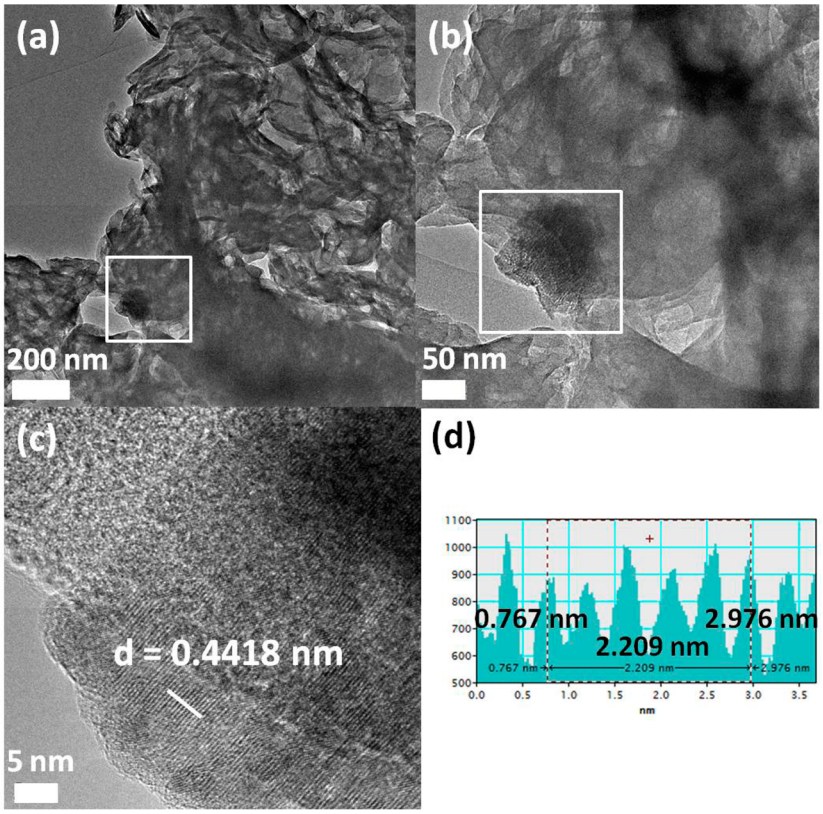

Figure 3. TEM (a, b), HR-TEM (c), and corresponding crystal lattice space (d) of a 3 wt % $Co(OH)_2$/g-C_3N_4 sample.

change after incorporation with a small amount of $Co(OH)_2$. The same result was also revealed in the XRD discussions. The enhanced optical absorption in the visible light region is mainly due to the loading of layered $Co(OH)_2$ on the surface of g-C_3N_4 and the reducing light-harvesting ability of the g-C_3N_4 host. Therefore, the excessive $Co(OH)_2$ loading on the substrate may not be in favor of photoredox catalysis. This hypothesis can be certified by the following photocatalytic experimental results. In Figure 4b, all of the samples show similar peaks centered at about 460 nm, with an obvious decrease in the peak intensity as the loading content increased. This is a good illustration that the recombination rate of the photogenerated charge carrier is enormously restrained due to the development of an adaptive heterojunction between g-C_3N_4 and $Co(OH)_2$.[17] When g-C_3N_4 was excited by visible light photons, a pair of photoinduced electrons and holes was generated, which then migrated from the bulk to the interface of the semiconductor and then to the side of $Co(OH)_2$ benefitting from the band-bending of the junction.[18] This could facilitates the heterogeneous photocatalysis.

To further reveal the properties of the developed $Co(OH)_2$/g-C_3N_4 hybridized material, electrochemical experiments were performed. Figure 5a shows the polarization curves of both pure and $Co(OH)_2$-optimized g-C_3N_4. The positive current in the range of 1.4−1.8 V vs Ag/AgCl can be ascribed to O_2 evolution.[19] Evidently, a much reduced overpotential can be found when $Co(OH)_2$ was engineered as a robust cocatalyst in comparison with pure g-C_3N_4. This is beneficial for promoting multiple-electron water oxidation kinetics and avoiding excessive driving potentials.

An electrochemical Nyquist plot experiment was also adopted. The charge transport resistances from EIS studies obtained by fitting the impedance spectra are 20141, 13924, and 7996 Ω for g-C_3N_4, Co_3O_4/g-C_3N_4, and $Co(OH)_2$/g-C_3N_4, respectively.[20] In Figure 5b, a remarkably decreased radius is found when a certain amount of $Co(OH)_2$ is decorated on g-C_3N_4. This predicts the optimized electrochemical impedance of the semiconductor when an adaptive g-C_3N_4/OEC junction is well created. Both of the electrochemical results imply that the creation of OEC active sites on the interface of g-C_3N_4 accelerates the charge carrier separation and migration and thus promotes the heterogeneous photocatalytic water oxidation process.

The photocatalytic performance of the as-prepared solids was therefore evaluated in an assay of the photocatalytic water oxidation reaction. In Figure 6a, it is clear that the OER is dramatically increased after loading $Co(OH)_2$ as an effective cocatalyst. The OER of pure g-C_3N_4 under UV−vis light irradiation (λ >300 nm) is 5 μmol h^{-1}. As the loading content of $Co(OH)_2$ increased, the OER significantly increased. When the loading content of $Co(OH)_2$ is 1 wt %, the OER is dramatically increased to 21 μmol h^{-1}, which is ca. 4 times higher than that of pristine g-C_3N_4. The optimum loading content is determined as 3 wt %, with the best oxygen evolution rate of 27.4 μmol h^{-1}. This value is 5.5 times higher than that of pristine g-C_3N_4. On further increase of the loading content to 5 wt %, the OER is decreased to 18 μmol h^{-1}; however, this is still much larger than that of pure g-C_3N_4. This is mainly due to the excessive loading of $Co(OH)_2$ that blocks the optical absorption of g-C_3N_4.

To further exhibit the promising properties of $Co(OH)_2$, we extended the photosensitizers to WO_3 and $BiVO_4$, which are widely regarded as the most efficient photoanode materials for catalyzing the water oxidation half-reaction in the overall water-splitting reaction by coupling with hydrogen-production photocathode semiconductors in Z-type photocatalytic and

DOI: 10.1021/cs502002u
ACS Catal. 2015, 5, 941−947

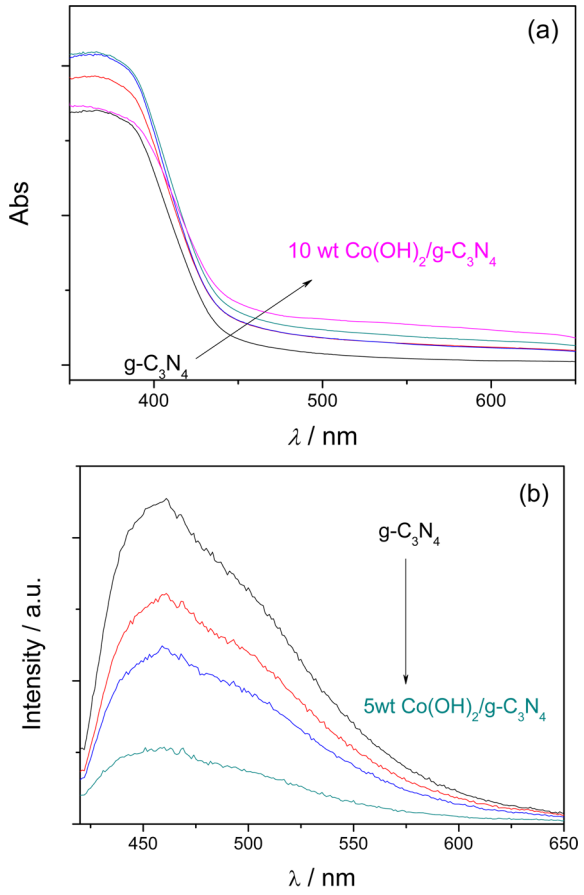

Figure 4. UV−vis DRS (a) and room-temperature PL (b) spectra for pure and $Co(OH)_2$-modified g-C_3N_4 samples.

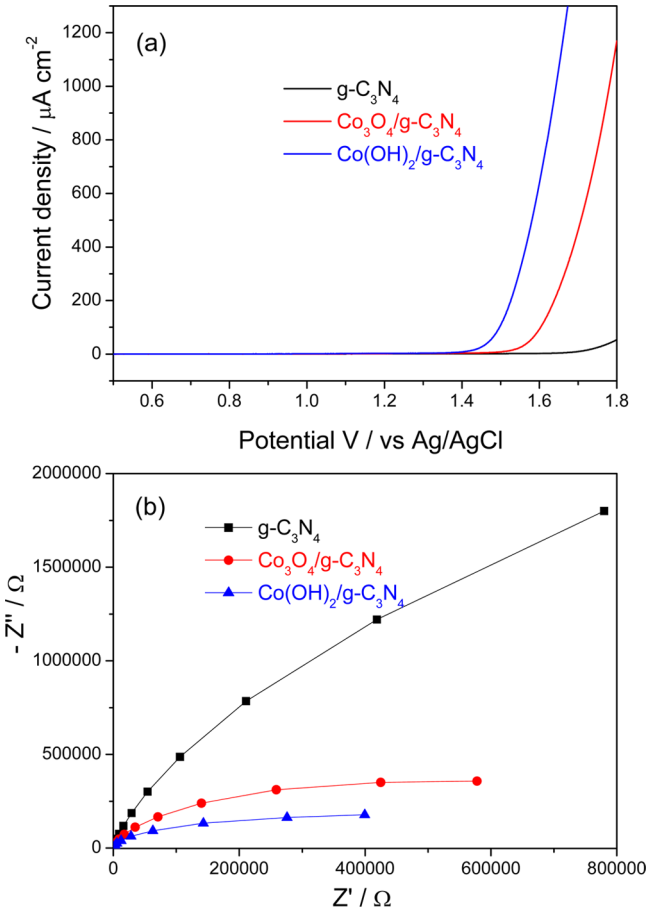

Figure 5. Polarization curves in the dark of CN, 3 wt % Co_3O_4/g-C_3N_4, and 3 wt % $Co(OH)_2$/g-C_3N_4 electrodes in 0.2 M Na_2SO_4 solution (a) and Nyquist plots of electrochemical impedance spectroscopy in the dark of g-C_3N_4, 3 wt % Co_3O_4/g-C_3N_4, and 3 wt % $Co(OH)_2$/g-C_3N_4 electrodes at 0.4 V vs Ag/AgCl (b).

photoelectrocatalytic systems (Figure S2, Supporting Information). It is observed that the same enhanced water oxidation rate was achieved under visible light irradiation (λ >420 nm). However, the enhanced water oxidation rate for both of the oxides (less than 0.5 times) is lower than that of g-C_3N_4 (4 times). Both the universality and the specificity of $Co(OH)_2$ have been illustrated to underline the importance of structural matching between the same layered crystals of host and guest materials. Interestingly, when a $Co(OH)_2$-modified inorganic/polymeric semiconductor was annealed at 300 °C in the air for 1 h, the water oxidation rate of the optimized material decreased. From the XRD analysis, after annealing treatment, the layered $Co(OH)_2$ was converted to Co_3O_4 nanoparticles (Figure S3, Supporting Information), which is commonly considered as an energetic cocatalyst for water oxidation. This emphasizes the dramatic photocatalytic performance of the layered $Co(OH)_2$ in comparison with that of Co_3O_4 under the same conditions. From the TEM picture, few differences can be seen after the thermal annealing treatment (Figure S4, Supporting Information).

In order to underline the importance of the cobalt hydroxide for water oxidation, we also investigated the behaviors of the other common transition-metal hydroxides as WOCs to drive the water oxidation reaction. As shown in Table 1, the same amounts of Fe^{3+}, Mn^{2+}, Ni^{2+}, and Cu^{2+} were adopted for in situ synthesis of the hydroxide/g-C_3N_4 samples under the same experimental conditions. It is interesting to observe that only $Mn(OH)_2$ and $Cu(OH)_2$ slightly enhanced the water oxidation performance, while $Fe(OH)_3$ and $Ni(OH)_2$ exhibited reduced water oxidation rates. This reveals the unique properties of cobalt hydroxide in accelerating the water oxidation reaction, which is mainly due to the convenient redox transformation of different chemical states (Co^{2+}, Co^{3+}, and Co^{4+}). Another advantage originating from the loading of the $Co(OH)_2$ for water oxidation is the enhanced selectivity for producing O_2. When pure g-C_3N_4 was adopted for water oxidation, oxygen evolution (5 μmol h^{-1}) was accompanied by nitrogen evolution (6 μmol h^{-1}). This is mainly due to photooxidation/photocorrosion of g-C_3N_4 as a result of the buildup of light-trigged charges on g-C_3N_4.[6d] The selectivity for oxygen evolution of pure g-C_3N_4 is 45%, while the selectivity is nearly 99% for $Co(OH)_2$ optimized g-C_3N_4. The O_2 selectivity for the other metal hydroxides has also been calculated. $Mn(OH)_2$ and $Cu(OH)_2$ modified g-C_3N_4 show a selectivity of 57.6 and 57%, while $Fe(OH)_3$ and $Ni(OH)_2$ show poor selectivity in comparison to pure g-C_3N_4 (32 and 42%), indicating $Co(OH)_2$ is superior in promoting O_2 evolution selectivity.

Furthermore, long time course water oxidation experiments were carried out under both UV and visible light irradiation. As shown in Figure 6b, the oxygen evolution rates (OER) were determined to be 27.4 and 7.1 μmol h^{-1} for UV−vis and visible light irradiation, respectively. The amounts of evolved gases reached 52 and 20 μmol after 7 and 9 h of persistent irradiation. The reduced OER is ascribed to the deposition of Ag particles on the surface of g-C_3N_4 (generated from the photoreduction

DOI: 10.1021/cs502002u
ACS Catal. 2015, 5, 941−947

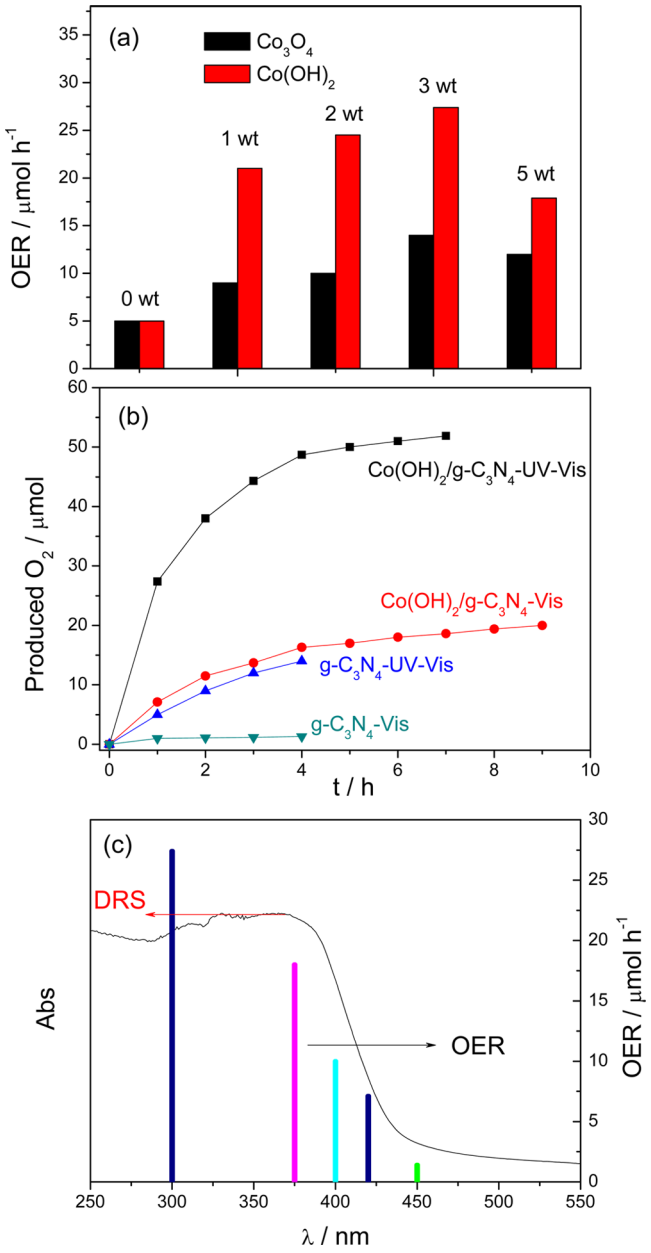

Figure 6. OER of Co_3O_4 and $Co(OH)_2$-modified g-C_3N_4 under UV−vis irradiation (λ >300 nm) (a), time course of produced O_2 for pure g-C_3N_4 and 3 wt % $Co(OH)_2$/g-C_3N_4 (b), and wavelength dependence of the O_2 evolution rate for 3 wt % $Co(OH)_2$/g-C_3N_4 (c) under visible and UV−vis irradiation.

Table 1. Effects of Different Transition Metals as Cocatalysts To Promote OER of g-C_3N_4 under UV−Vis Irradiation (λ >300 nm)

entry	cocatalyst	amt of cocatalyst/wt %	OER/ μmol h^{-1}	NER/ μmol h^{-1}	O_2 selectivity
1			5	3.7	57
2	$Co(OH)_2$	3	27.4	2.8	91
3	$Mn(OH)_2$	3	7.2	5.3	57.6
4	$Fe(OH)_3$	3	2.4	5.2	32
5	$Cu(OH)_2$	3	6.8	5.1	57
6	$Ni(OH)_2$	3	3.6	5	42

of Ag^+) that leads to the light shading effect and hinders the optical absorption.[10a] We have evaluated the oxygen evolution rate (OER) of the 3 wt % $Co(OH)_2$/g-C_3N_4 sample under different specific wavelength illuminations.[21] As shown in Figure 6c, the OER of the samples is associated with the DRS absorption spectra. When the illumination wavelengths are λ >300, 375, 400, 420, and 450 nm, the OER values are 27.4, 18, 10, 7.1, and 1.4 μmol h^{-1}, respectively. This indicates that the photocatalytic oxygen evolution reaction is indeed promoted by the photons. The recycle ability of the samples has also been determined (Figure S6, Supporting Information). The activity of the recycled sample shows a slightly reduced rate, which is mainly due to the loading of Ag nanoparticles on the surface of the substrate material. This can be further verified by the XRD, DRS, TEM, and XPS characterizations of the recycled catalyst (Figures S7 and S8, Supporting Information).

CONCLUSION

In this paper, we have successfully synthesized an adaptive $Co(OH)_2$/g-C_3N_4 junction. This cheap and easy incorporation of $Co(OH)_2$ significantly restrains the recombination rate of the interface charge carriers, reduces the huge energy barrier for O−O bond formation, and accelerates the oxygen evolution kinetics. The optimum water oxidation rates of the modified sample are 27.4 and 7.1 μmol h^{-1} under UV and visible light irradiation, respectively, which are 5.5 and 7 times larger than that of the pristine g-C_3N_4. Such structure and morphology engineering not only optimizes the optical, electrical, and texture properties of the hybrid materials for water oxidation to liberate dioxygen into the atmosphere but also provides ideas for designing novel materials by incorporating different available materials with polymeric g-C_3N_4. Thus, it is essential to extend their functions to wide applications, including CO_2 reduction, pollution purification, and fine chemical synthesis.

ASSOCIATED CONTENT

Supporting Information

The following file is available free of charge on the ACS Publications website at DOI: 10.1021/cs502002u (PDF).

OER for $Co(OH)_2$ modified semiconductors and XRD, BET, DRS, XPS, and TEM characterizations for $Co(OH)_2$ loaded g-C_3N_4

AUTHOR INFORMATION

Corresponding Author

*E-mail for X.W.: xcwang@fzu.edu.cn.

Notes

The authors declare no competing financial interest.

ACKNOWLEDGMENTS

This work has been financially supported by the National Basic Research Program of China (2013CB632405), the National Natural Science Foundation of China (21425309 and 21173043), the State Key Laboratory of NBC Protection for Civilian (SKLNBC2013-04K), the Specialized Research Fund for the Doctoral Program of Higher Education (20133514110003), and the Department of Education of Fujian Province in the People's Republic of China.

REFERENCES

(1) (a) Fujishima, A.; Honda, K. *Nature* **1972**, *238*, 37−38. (b) Maeda, K.; Teramura, K.; Lu, D.; Takata, T.; Saito, N.; Inoue, Y.; Domen, K. *Nature* **2006**, *440*, 295. (c) Chen, X. B.; Shen, S. H.;

DOI: 10.1021/cs502002u
ACS Catal. 2015, 5, 941−947

Guo, L. J.; Mao, S. S. *Chem. Rev.* **2010**, *110*, 6503−6570. (d) Zou, Z. G.; Ye, J. H.; Sayama, K. *Nature* **2001**, *414*, 625−627.
(2) (a) Kudo, A.; Miseki, Y. *Chem. Soc. Rev.* **2009**, *38*, 253−278. (b) Lewis, N. S.; Nocera, D. G. *Proc. Natl. Acad. Sci. U.S.A.* **2006**, *103*, 15729−15735. (c) Ran, J. R.; Zhang, J.; Yu, J. G.; Jaroniecc, M.; Qiao, S. Z. *Chem. Soc. Rev.* **2014**, *43*, 7787−7812.
(3) (a) Maeda, K.; Xiong, A.; Yoshinaga, T.; Ikeda, T.; Sakamoto, N.; Hisatomi, T.; Takashima, M.; Lu, D.; Kanehara, M.; Setoyama, T.; Teranishi, T.; Domen, K. *Angew. Chem., Int. Ed.* **2010**, *122*, 4190−4193. (b) Kanan, M. W.; Nocera, D. G. *Science* **2008**, *321*, 1072−1075. (c) Gao, M. R.; Xu, Y. F.; Jiang, J.; Zheng, Y. R.; Yu, S. H. *J. Am. Chem. Soc.* **2012**, *134*, 2930−2933. (d) Pfrommer, J.; Lublow, M.; Azarpira, A.; Göbel, C.; Lücke, M.; Steigert, A.; Pogrzeba, M.; Menezes, P. W.; Fischer, A.; Schedel-Niedrig, T.; Driess, M. *Angew. Chem., Int. Ed.* **2014**, *53*, 5183−5187.
(4) (a) Lalrempuia1, R.; McDaniel, N.; Müller-Bunz1, H.; Bernhard, S.; Albrecht, M. *Angew. Chem., Int. Ed.* **2010**, *49*, 9765−9768. (b) Hull, J.; Balcells, D.; Blakemore, J.; Incarvito, C.; Eisenstein, O.; Brudvig, G.; Crabtree, R. *J. Am. Chem. Soc.* **2009**, *131*, 8730−8731. (c) McDaniel, N.; Coughlin, F.; Tinker, L.; Bernhard, S. *J. Am. Chem. Soc.* **2008**, *130*, 210−217.
(5) Walter, M. G.; Warren, E. L.; McKone, J. R.; Boettcher, S. W.; Mi, Q.; Santori, E. A.; Lewis, N. S. *Chem. Rev.* **2010**, *110*, 6446−6473.
(6) (a) Zhong, D. K.; Gamelin, D. R. *J. Am. Chem. Soc.* **2010**, *132*, 4202−4207. (b) Jiao, F.; Frei, H. *Energy Environ. Sci.* **2010**, *3*, 1018−1027. (c) Wang, D.; Li, R.; Zhu, J.; Shi, J.; Han, J.; Zong, X.; Li, C. *J. Phys. Chem. C* **2012**, *116*, 5082−5089. (d) Zhang, J.; Grzelczak, M.; Hou, Y. D.; Maeda, K.; Domen, K.; Fu, X. Z.; Wang, X. C. *Chem. Sci.* **2012**, *3*, 443−446.
(7) Lin, F.; Boettcher, S. W. *Nat. Mater.* **2014**, *13*, 81−86.
(8) Kim, T. W.; Choi, K. *Science* **2014**, *343*, 990−994.
(9) (a) Wang, X. C.; Maeda, K.; Thomas, A.; Takanabe, K.; Xin, G.; Carlsson, J. M.; Domen, K.; Antonietti, M. *Nat. Mater.* **2009**, *8*, 76−82. (b) Goettmann, F.; Thomas, A.; Antonietti, M. *Angew. Chem., Int. Ed.* **2007**, *46*, 2717−2720. (c) Thomas, A.; Fischer, A.; Goettmann, F.; Antonietti, M.; Müller, J. O.; Schlögl, R.; Carlsson, J. M. *J. Mater. Chem.* **2008**, *18*, 4893−4908.
(10) (a) Maeda, K.; Wang, X. C.; Nishihara, Y.; Lu, D.; Antonietti, M.; Domen, K. *J. Phys. Chem. C* **2009**, *113*, 4940−4947. (b) Zhang, G. G.; Zhang, M. W.; Ye, X. X.; Qiu, X. Q.; Lin, S.; Wang, X. C. *Adv. Mater.* **2014**, *26*, 805−809. (c) Zhang, J. S.; Sun, J. H.; Maeda, K.; Domen, K.; Liu, P.; Antonietti, M.; Fu, X. Z.; Wang, X. C. *Energy Environ. Sci.* **2011**, *4*, 675−678. (d) Liu, G.; Niu, P.; Sun, C.; Smith, S.; Chen, Z.; Lu, G. Q.; Cheng, H. *J. Am. Chem. Soc.* **2010**, *132*, 11642−11648. (e) Hong, J.; Xia, X.; Wang, Y.; Xu, R. *J. Mater. Chem.* **2012**, *22*, 15006−15012.
(11) (a) Wang, S. B.; Lin, J. L.; Wang, X. C. *Phys. Chem. Chem. Phys.* **2014**, *16*, 14656−14660. (b) Lin, J. L.; Pan, Z. M.; Wang, X. *ACS Sustainable Chem. Eng.* **2014**, *2*, 353−358. (c) Hong, J. D.; Zhang, W.; Wang, Y. B.; Zhou, T. H.; Xu, R. *ChemCatChem* **2014**, *6*, 2315−2321.
(12) (a) Chen, X. F.; Zhang, J. S.; Fu, X. Z.; Antonietti, M.; Wang, X. C. *J. Am. Chem. Soc.* **2009**, *131*, 11658−11659. (b) Ye, X. J.; Cui, Y. J.; Qiu, X. Q.; Wang, X. C. *Appl. Catal., B* **2014**, *152*, 383−389.
(13) (a) Lin, Z. Z.; Wang, X. C. *Angew. Chem., Int. Ed.* **2013**, *52*, 1735−1738. (b) Zhang, G. G.; Wang, X. C. *J. Catal.* **2013**, *307*, 246−253. (c) Zhang, M. W.; Wang, X. C. *Energy Environ. Sci.* **2014**, *7*, 1902−1906.
(14) (a) Yang, J.; Liu, H. W.; Martens, W. N.; Frost, R. L. *J. Phys. Chem. C* **2010**, *114*, 111−119. (b) Liu, X. H.; Ma, R. Z.; Bando, Y.; Sasaki, T. *Adv. Funct. Mater.* **2014**, *24*, 4292−4302. (c) Chu, S.; Wang, Y.; Guo, Y.; Feng, J.; Wang, C.; Luo, W.; Fan, X.; Zou, Z. G. *ACS Catal.* **2013**, *3*, 912−919.
(15) (a) Lyth, S. M.; Nabae, Y.; Moriya, S.; Kuroki, S.; Kakimoto, M.; Ozaki, J.; Miyata, S. *J. Phys. Chem. C* **2009**, *113*, 20148−20151. (b) Wang, X. C.; Blechert, S.; Antonietti, M. *ACS Catal.* **2012**, *2*, 1596−1606.
(16) (a) Foy, D. *J. Solid State Chem.* **2009**, *182*, 165−171. (b) Zhang, J. S.; Zhang, M. W.; Zhang, G. G.; Wang, X. C. *ACS Catal.* **2012**, *2*, 940−948.
(17) (a) Xiang, Q. J.; Yu, J. G.; Jaroniec, M. *J. Phys. Chem. C* **2011**, *115*, 7355−7363. (b) Zhang, X. H.; Yu, L. J.; Zhuang, C. S.; Peng, T. Y.; Li, R. J.; Li, X. G. *ACS Catal.* **2014**, *4*, 162−170.
(18) (a) Niu, P.; Liu, G.; Cheng, H. M. *J. Phys. Chem. C* **2012**, *116*, 11013−11018. (b) Zhang, H. Y.; Yu, A. C. *J. Phys. Chem. C* **2014**, *118*, 11628−11635.
(19) (a) Hou, Y. D.; Laursen, A. B.; Zhang, J. S.; Zhang, G. G.; Zhu, Y. S.; Wang, X. C.; Dahl, S.; Chorkendorff, Ib. *Angew. Chem., Int. Ed.* **2013**, *52*, 3621−3625. (b) Mansor, N.; Jorge, A. B.; Corà, F.; Gibbs, C.; Jervis, R.; McMillan, P. F.; Wang, X.; Brett, D. J. L. *J. Phys. Chem. C* **2014**, *118*, 6831−6838.
(20) (a) Zhou, F. L.; Li, X. J.; Shu, J.; Wang, J. *J. Photochem. Photobiol. A: Chem.* **2011**, *219*, 132−138. (b) Leng, W. H.; Zhang, Z.; Zhang, J. Q.; Cao, C. N. *J. Phys. Chem. B* **2005**, *109*, 15008−15023.
(21) Gu, J.; Yan, Y.; Krizan, J. W.; Gibson, Q. D.; Detweiler, Z. M.; Cava, R. J.; Bocarsly, A. B. *J. Am. Chem. Soc.* **2014**, *136*, 830−833.

DOI: 10.1021/cs502002u
ACS Catal. 2015, 5, 941−947